

# CMTNet: Convolutional Meets Transformer Network for Hyperspectral Images Classification

Faxu Guo, Quan Feng, Sen Yang, and Wanxia Yang .

**Abstract**—Hyperspectral remote sensing (HIS) enables the detailed capture of spectral information from the Earth’s surface, facilitating precise classification and identification of surface crops due to its superior spectral diagnostic capabilities. However, current convolutional neural networks (CNNs) primarily focus on local features in hyperspectral data, leading to suboptimal performance when classifying intricate crop types and addressing imbalanced sample distributions. In contrast, the Transformer framework excels at extracting global features from hyperspectral imagery. To leverage the strengths of both approaches, this research introduces the Convolutional Meet Transformer Network (CMTNet). This innovative model includes a spectral-spatial feature extraction module for shallow feature capture, a dual-branch structure combining CNN and Transformer branches for local and global feature extraction, and a multi-output constraint module that enhances classification accuracy through multi-output loss calculations and cross-constraints across local, global, and joint features. Extensive experiments conducted on three datasets (WHU-Hi-LongKou, WHU-Hi-HanChuan, and WHU-Hi-HongHu) demonstrate that CMTNet significantly outperforms other state-of-the-art networks in classification performance, validating its effectiveness in hyperspectral crop classification.

**Index Terms**—Hyperspectral imaging, crop classification, multi-output feature constraints, convolutional neural networks, transformer.

## I. INTRODUCTION

Accurate identification of crop types is crucial for agricultural monitoring, crop yield estimation, growth analysis, and determining the spatial distribution and area of crops [1]. It also provides essential reference information for resource allocation, agricultural structure adjustment, and the formulation of economic development strategies in the agricultural production process. In recent years, with the continuous improvement of spectral imaging technology, hyperspectral imaging (HSI) has become a research hotspot for remote sensing data analysis [2, 3]. HSI images consist of dozens or hundreds of spectral channels containing abundant spectral and spatial information. The high spatial resolution of HSI provides new opportunities for detecting subtle spectral differences between crops, which is beneficial for the fine classification of crops. In addition, HSI is widely used in areas such as plant disease

detection [4], food inspection [5], re-identification [6], and geological exploration [7].

Traditional methods for HIS classification typically include designed loss [8] and designed model [9]. In addition, scholars have also introduced several methods for HIS spectral dimension reduction and information extraction, including principal component analysis, minimum noise fraction transformation, linear discriminant analysis, independent component analysis, and others. However, these methods only consider the spectral information of HIS, ignoring the spatial correlation between pixels in the spatial dimension. This overlooks the spatial features contained in HIS data and ignored rich spatial contextual information, leading to variability in the spectral features of target objects, thereby affecting the classification performance. To utilize spatial information in the images, scholars have studied various mathematical morphology operators suitable for HIS to extract spatial features from the images, including morphological profile features, extended morphological profile features, extended multi-attribute profile features (EMAP), and extinction profile features [10, 11]. Although hyperspectral image classification methods based on spatial features can effectively capture the spatial information such as the position, structure, and contours of target objects, they neglect the spectral dimension information of hyperspectral remote sensing images, resulting in less-than-ideal classification results. The generalization and versatility of traditional HIS classification methods are weak, and they are susceptible to salt-and-pepper noise, which affects classification accuracy.

In recent years, many deep learning-based methods have been applied to HIS classification [12, 13], as illustrated in Fig.1. Initially, deep belief networks (DBN) [14], recurrent neural networks (RNN) [15], and one-dimensional convolutional neural networks (1D-CNN) [16] was introduced into the HIS classification field. However, these methods only utilize spectral information and ignore the neighborhood information in the spatial dimension, leading to lower classification accuracy [17]. To address this issue, researchers proposed an architecture based on two-dimensional convolutional neural networks (2D-CNN) [18]. Subsequently, Xu et al. [19] combined 1D-CNN and 2D-CNN, constructing a dual-branch network structure to extract spectral and spatial features. However, this approach extracts spectral and spatial features separately and cannot effectively utilize the 3D spectral-spatial features of HIS. In order to better extract spectral-spatial features, researchers developed the 3D-CNN [18] architecture and applied it to HIS classification. To overcome the limitation of CNN in capturing global information, scholars have proposed two

This research was funded by National Natural Science Foundation of China (32160421), Higher Education Industry Support Program of Gansu Province(2021CYZC-57) and the Youth Doctoral Fund of Gansu Province(2021QB-033).(Corresponding author: Quan Feng)

Faxu Guo, Quan Feng, Sen Yang, and Wanxia Yang are with the College of Mechanical and Electrical Engineering, Gansu Agriculture University, Lanzho163u 730070, China (e-mail: guofax@gsau.edu.cn; fqan@gsau.edu.cn; yangsen@gsau.edu.cn; yangwanxia@163.com)

approaches to improve CNN. One approach is to enhance the perceptual directly range of the convolutional kernel, including the use of dilated convolutions [20] and building a multi-scale feature pyramid [21]; the other method is to embed an attention module [22] that can capture global contextual information into the CNN structure [23, 24], including spectral attention, spatial attention, and spatiotemporal attention. However, these methods still rely on convolutional operations in the backbone network to encode dense features, thus tending to local semantic information interaction [25]. Capturing long-range dependencies becomes a pivotal breakthrough to overcome the performance bottleneck of CNN.

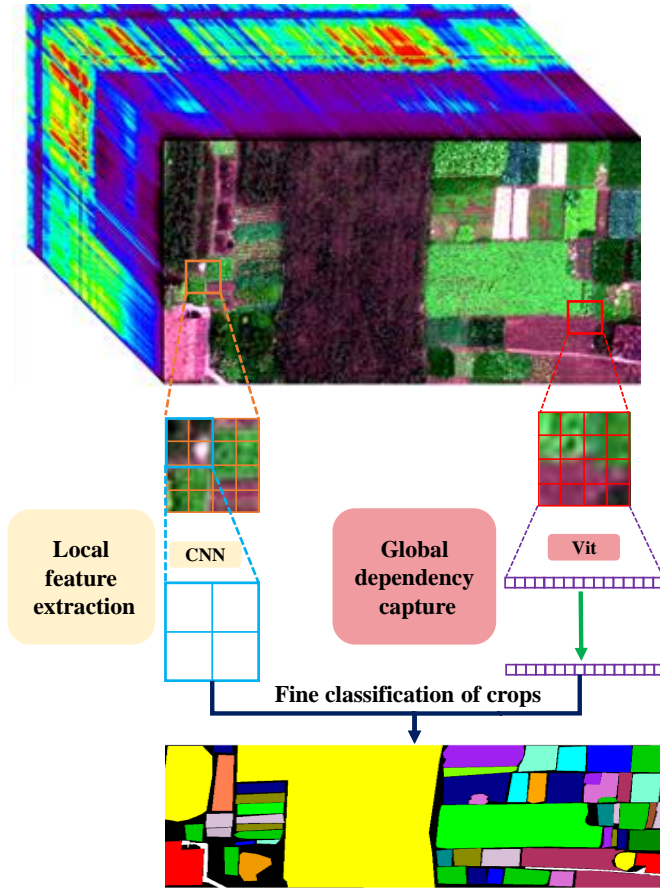


Fig. 1. HSI classification using deep learning approach.

Recently, a visual transformer (ViT) [26] has been applied to various image processing tasks and has been preliminarily applied to the HSI classification field [27]. ViT originates from the field of natural language processing (NLP) and is a new type of deep neural network composed of a multi-head attention mechanism and feedforward neural network, which can capture long-range dependency relationships in sequences through the multi-head attention mechanism [28, 29]. Compared to CNN, the self-attention mechanism of the Transformer imitates the saliency detection and selective attention of biological vision, and can establish long-distance

dependency relationships, solving the limited receptive field problem of convolutional neural networks [30]. However, ViT is not good at capturing local features. Given this, some scholars have begun to combine CNN and ViT to capture local jointly information, sequence features, and long-range dependency relationships. Existing HSI classification methods based on CNN-Transformer hybrid architectures [25] usually adopt manually specified hybrid strategies, such as using convolution to extract local features in the shallow layers and using a Transformer to extract global features in the deep layers [29, 31], or directly adding the features extracted by CNN and Transformer [32]. However, these methods are challenging to meet the recognition requirements of fine-grained materials in various complex hyperspectral scenes. In some agricultural scenes, the spatial shapes and spectral patterns between different crops are more similar in global features, and they rely more on local features such as texture to identify the types of materials, while the Transformer degrades high-frequency signals, making it challenging for the model to learn distinctive features.

Therefore, this study introduces a novel hyperspectral crop classification approach utilizing the Convolutional transform dual-branch feature extraction network (CTDBNet). The model leverages a combination of 3D and 2D convolutional layers to extract shallow spectral-spatial features, thereby mitigating feature redundancy and inaccuracies associated with deep layers. Furthermore, a dual-branch architecture comprising CNN and Transformer components is employed to extract comprehensive local-global features. Additionally, a multi-output constraint module is introduced to effectively integrate advanced semantic features.

The main contributions of this article are given as follows.

- A spectral-spatial feature extraction module was developed, consisting of a 3D convolutional layer followed by a 2D convolutional layer to extract shallow spectral spatial features.
- To leverage the high-level semantic features obtained from the CNN and Transformer branches, a multi-output constraint module was implemented to fully utilize the extracted features.
- The proposed CTDBNet, utilizing a dual-branch structure with CNN and Transformer, aims to extract both local and global spectral spatial features. Experimental results on three datasets show that our method outperforms some state-of-the-art networks based on CNN and Transformer, indicating its potential for further improvements.

## II. RELATED WORK

### A. CNN-Based Methods

CNN is a powerful tool for analyzing HIS images because they can accurately represent the spectral and spatial contextual information contained in the HIS data cube, extracting highly abstract features from the raw data and achieving excellent classification results. HIS classification tasks are categorized into three based on the distinct features CNN

processes. The initial category involves 1D-CNN, focusing on spectral features. The data input for 1D-CNN is typically a single pixel. Li et al. [33] proposed a feature extraction module and feature interaction in the frequency domain to enhance salient features. Chen et al. [34] used a multi-layer convolutional network to extract deep features of HIS, improving the classification results with a few training samples. Yue et al. [35] utilized principal component analysis for HIS preprocessing before feature extraction. The second category involves 2D-CNN, focusing on spatial features. Li et al. [36] used two 2D-CNN networks to extract high spectral and spatial frequency information simultaneously. Zhao et al. [37] proposed a 2D-CNN model that initially reduces dimensionality using PCA or another method, followed by data input into the model, where the data undergo initial processing by 2D-CNN to extract spatial information, subsequently combined with spectral information. Haut et al. [38] developed a novel classification model guided by active learning, employing a Bayesian approach. The last category is based on spectral-spatial feature methods. In this case, there are two ways of feature processing. One approach involves the use of 3D-CNN. For instance, Li et al. [39] introduced a 3D-CNN framework for the efficient extraction of deep spectral-spatial combined features from HSI cube data without preprocessing or post-processing. Another approach involves hybrid CNN, with significant research applying this method [40–42]. Xu et al. [19] integrated multi-source remote sensing data to enhance classification performance, employing 1D-CNN and 2D-CNN for the extraction of spectral and spatial features, respectively. Diakite et al. [43] suggested a hybrid network combining 3D-CNN and 2D-CNN. However, the current CNN-based methods overlook important differences between spatial pixels and unequal contributions of spectral bands. Convolutional kernels with limited receptive fields are independent of content, resulting in less accurate recognition of ground objects with local contextual similarity and large-scale variations.

Subsequently, the attention mechanism has been widely integrated with CNN frameworks [40, 44–46] due to its capability to assign varying weights to input features, enabling the model to concentrate more on crucial task-related information. Haut et al. [47] introduced a dual data-path attention module as the basic building block, considering both bottom-up and top-down visual factors to enhance the network’s feature extraction capability. Liu et al. [40], based on the widely used convolutional block attention module (CBAM) improved accuracy by changing the way the attention module is connected. Tang et al. [48] presented two attention models from spatial and spectral dimensions to emphasize crucial spatial regions and specific spectral bands, offering significant information for the classification task. Additionally, Roy et al. [49] suggested an attention-based adaptive spectral-spatial kernel to enhance the residual network, capturing discriminative spectral-spatial features through end-to-end training for HSI classification. These attention-based methods are essentially enhanced versions of CNN, yet they are restricted by the inherent constraints of local convolutional kernels. These approaches emphasize local

features while neglecting global information, consequently inadequately addressing the remote dependency between spectral sequences and spatial pixels.

### B. Transformer-Based Methods

The initial design of the Transformer was focused on sequence modeling and transduction tasks. Its remarkable success in natural language processing has prompted researchers to explore its application in the visual domain, where it has demonstrated exceptional performance in tasks such as image classification and joint visual-linguistic modeling. Encouraged by the achievements of the Vis-Transformer, many researchers have extended the use of the Transformer to HSI classification tasks. In their work, Hong et al. [50] were the first to apply the ViT to HIS classification and achieved impressive results on commonly used hyperspectral image datasets. Additionally, He et al. [51] utilized a well-trained bidirectional encoder transformer structure for hyperspectral image classification. Furthermore, Qing et al. [52] introduced the self-attention-based transformer network (SAT-Net) for HSI classification, employing multiple Transformer encoders to extract image features. The encoder modules are directly connected using a multi-level residual structure to address the issues of vanishing gradients and overfitting. Tan et al. [53] introduced the transformer-in-transformer module for end-to-end classification, building a deep network model that fully utilizes global and local information in the input spectral cube. Sun et al. [24] proposed the spatial and spectral attention mechanism fusion network (SSAMF) for HSI classification, which incorporates channel self-attention into the Swin Transformer to better encode the rich spectral-spatial information of HSI, contributing to improved classification by the network. Mei et al. [54] proposed the Group-Aware Hierarchical Transformer (GAHT) for HIS classification, applying multi-head self-attention to local spatial-spectral context and hierarchically constructing the network to improve classifying accuracy. Zhong et al. [55] developed a spectral-spatial transformer network (SSTN) to overcome the constraints of convolutional kernels. Additionally, stable and efficient network architecture optimization is achieved through fast architecture search. It is evident that these previous studies primarily utilize Transformer to learn strong interactions between comprehensive label information through multiple self-attention modules. However, they are troubled by slow processing speed during inference and high memory usage, and these methods have yet to exploit the rich spatial features of HIS fully.

### C. Hybrid Methods

Recently, multiple endeavors have sought to integrate CNN and Transformer to build HSI classification networks that leverage the strengths of both architectures. Zhang et al. [56] proposed a dual-branch structure, incorporating both CNN and Transformer branches to capture local-global hyperspectral features. In the multi-head self-attention mechanism, convolutional operations were introduced skillfully to unite CNN and Transformer, further enhancing the classification

progress. Liang et al. [57] integrated multi-head self-attention mechanisms in the spatial and spectral domains, applying them to context through uniform sampling and embedding 1D-CNN and 2D-CNN operations. Yang et al. [58] integrated CNN and Transformer sequentially and in parallel to fully utilize the features of HSI. Qi et al. [31] developed the global-local spatial convolution transformer (GACT) to exploit local spatial context features and global interaction between different pixels. Additionally, through the weighted multi-scale spectral-spatial feature interaction (WMSFI) module, trainable adaptive fusion of multi-scale global-local spectral-spatial information is achieved. Song et al. [38] presented a dual-branch HSI classification framework utilizing 3D-CNN and bottleneck spatial-spectral transformer (B2ST), where both branches use a combination of shallow CNN and deep Transformer. Yang et al. [59] embedded CNN operations into the Transformer structure to capture subtle spectral differences and convey local spatial context information, then encoded spatial-spectral representation along multiple dimensions through a novel convolution displacer. However, these methods are mainly derived from natural image processing experience and exhibit significant differences from low spatial resolution HSI. Effectively integrating the capability of CNN in local context exploration and the ability of Transformer in global modeling on spectral and spatial dimensions, as well as achieving adaptive fusion of spectral-spatial features with multiple attributes and scales still need to be solved.

### III. PROPOSED METHOD

The proposed method CTDBNet's framework is illustrated in Fig. 2. CTDBNet comprises a spectral-spatial feature extraction module, a local-global feature extraction module, and a multi-scale output constraint module. The spectral-space feature extraction module initially extracts shallow features from hyperspectral images by solely utilizing the spectral-space information present in the images. Subsequently, a parallel local-global feature extraction module, consisting of a Transformer branch and a CNN branch, is employed to deeply extract local and global features from the hyperspectral images. Finally, the classification results are generated using the multi-output constraint module, which calculates multi-output losses and cross-constraints on local, global, and joint features from various feature perspectives.

#### A. Spectral-Spatial Feature Extraction Module

The structure of the spectral-spatial feature extraction module outlined in this study is illustrated in Fig. 1. This module primarily utilizes convolutional neural networks to process the segmented hyperspectral image block. It begins by employing a 3D convolutional layer to extract spectral-spatial features, followed by a 2D convolutional layer to capture shallow spatial features. Let the hyperspectral dataset be denoted as  $H \in \mathbb{R}^{h \times w \times d}$ , with the spatial dimensions' height and width represented as  $h$  and  $w$ , respectively, and the number of spectral bands as  $d$ . Each pixel in  $H$  comprises  $d$  spectral dimensions, with its corresponding class label vector denoted

as  $V = (v_1, v_2, \dots, v_n)$ , where  $n$  signifies the number of land cover categories in the hyperspectral scene. To manage the extensive hyperspectral image data, block division is necessary during model training to accommodate the computer's computational limitations. Following partitioning, each hyperspectral image block is denoted as  $X \in \mathbb{R}^{m \times m \times d}$ , with its dimensions specified. Each training image block sample is then inputted into the initial 3D convolutional layer. The convolution kernel within the 3D convolution calculates new convolutional feature maps by summing the dot product between the convolution of the entire spatial dimension and the kernel. The calculation formula is presented in equation (1):

$$v_{i,j}^{p,q,u} = \sum_{\eta=1}^{\eta} \sum_{h=0}^h \sum_{w=0}^w \sum_{c=0}^c \omega_{i,j,\eta}^{h,w,c} \times v_{i-1,\eta}^{(p+h),(q+w),(u+c)} + b_{i,j} \quad (1)$$

Where  $\eta$  represents the feature related to the  $j$ -th convolutional feature cube of the  $i-1$  th layer;  $v_{i,j}^{p,q,u}$  represents the convolution output value at position  $(p, q, u)$  of the  $j$ -th convolutional feature cube of the  $i$ -th layer, with the convolution kernel size of  $(h, w, c)$ ;  $\omega_{i,j,\eta}^{h,w,c}$  and  $b_{i,j}$  represent the weight parameters and bias at position  $(h, w, c)$  related to the  $\eta$ -th convolutional feature cube.

Similar to the 3D convolutional layer, the 2D convolutional layer operates by convolving a two-dimensional kernel to produce new feature maps. The calculation formula for this process is depicted in equation (2):

$$v_{i,j}^{p,q} = \sum_{\eta=1}^{\eta} \sum_{h=0}^h \sum_{w=0}^w \omega_{i,j,\eta}^{h,w} \times v_{i-1,\eta}^{(p+h),(q+w)} + b_{i,j} \quad (2)$$

$v_{i,j}^{p,q}$  represents the convolution output value at position  $(p, q)$  of the  $j$ -th convolutional feature cube of the  $i$ -th layer, with the convolution kernel size of  $(h, w)$ ;  $(h, w)$ ;  $\omega_{i,j,\eta}^{h,w}$  and  $b_{i,j}$  represent the weight parameters and bias at position  $(h, w)$  related to the  $\eta$ -th convolutional feature cube.

This module consists of two convolutional layers, two batch normalization layers, and two activation layers using the ReLU activation function. The extraction process and calculation formulas of this module are detailed in equations (3) and (4):

$$v_{i,j}^{p,q} = \Phi(g_1(v_{i,j}^{p,q,u})) \quad (3)$$

$$y = \Phi(g_2(v_{i,j}^{p,q})) \quad (4)$$

Where  $\Phi(\bullet)$  represents the ReLU activation function,  $g_1$  and  $g_2$ , respectively, represent three-dimensional batch normalization and two-dimensional batch normalization.

#### B. Local-Global Feature Extraction Module

1) Transformer Encoder Branch: As shown in Fig. 2, the Transformer encoder branch mainly consists of positional encoding embeddings, multi-head self-attention (MHSA) (Fig. 3a), a multilayer perceptron (MLP), and two normalization layers. Residual connections are designed in front of MHSA and MLP. The output features of the spectral-spatial feature extraction module are flattened and linearly mapped to a

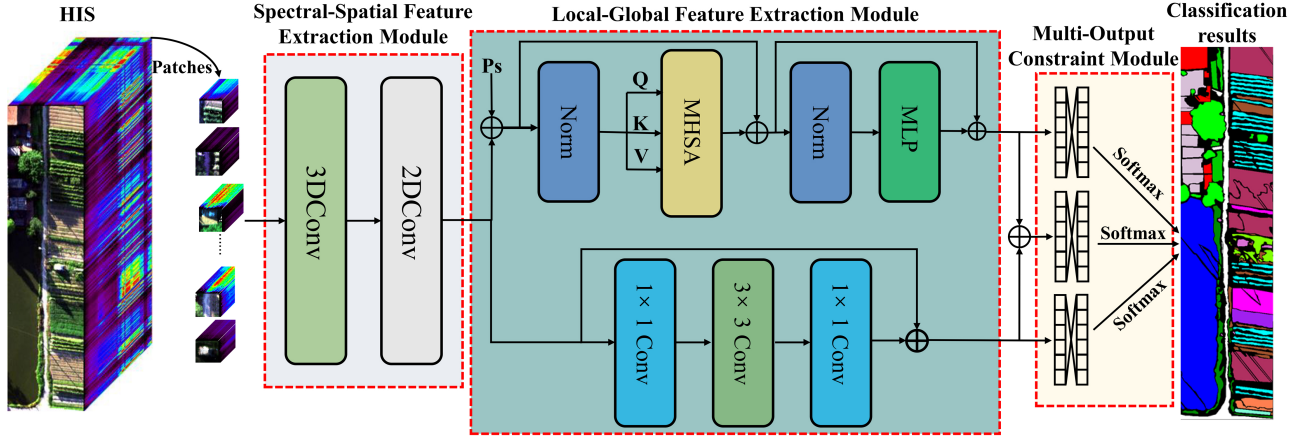


Fig. 2. CTDBNet overall network framework. CTDBNet consists of three main modules, spectral-spatial feature extraction module, local-global feature extraction module and multi-output constraint module.

sequence vector  $T \in \mathbb{R}^{n \times z}$  of length  $s$  and channel dimension  $z$ . Then, a relative positional information vector  $P_s \in \mathbb{R}^{n \times z}$  of length  $s$  is embedded into  $N$  sequence vectors as the input feature  $T_{in}$  of the Transformer encoder branch.

$$T_{in} = [T^1; T^2; \dots; T^N] + P_s \quad (5)$$

The Transformer encoder's exceptional performance can be attributed to its MHSA mechanism. MHSA efficiently captures the relationships between feature sequences by utilizing self-attention (SA) (see Fig. 3b). Initially, the  $Q$ ,  $K$ , and  $V$  values derived from the convolution mapping are passed to MHSA via SA to extract global features. Within this process,  $Q$  and  $K$  are used to calculate attention scores, and the softmax function is applied to determine the weights of these attention scores. The formula for SA can be expressed as follows:

$$T_{SA} = \text{Attention}(Q, K, V) = \text{soft max} \left( \frac{QK^T}{\sqrt{d_k}} \right) V \quad (6)$$

Where  $T_{SA}$  represents the output of the SA module, and  $d_k$  is the dimension of  $k$ . MHSA uses multiple sets of weight matrices to generate  $Q$ ,  $K$ , and  $V$ , and through a consistent computation process, multiple attention distributions are obtained. These distributions are then aggregated to obtain a comprehensive attention value. Finally, the features obtained by MHSA are passed to the MLP layer.

2) CNN Branch: As shown in Fig. 2, the CNN branch mainly consists of a 3x3 convolutional layer, two 1x1 convolutional layers, and residual connections, aiming to extract local features of hyperspectral images.

### C. Multi-Output Constraint Module

When calculating the loss, traditional feature constraints are only applied to the highest-level features of the network output. However, in hyperspectral image classification, high-level spatial and spectral semantic features contain valuable information. This study aims to preserve this critical information during multi-scale feature fusion by examining the impact of different features on classification performance. To achieve

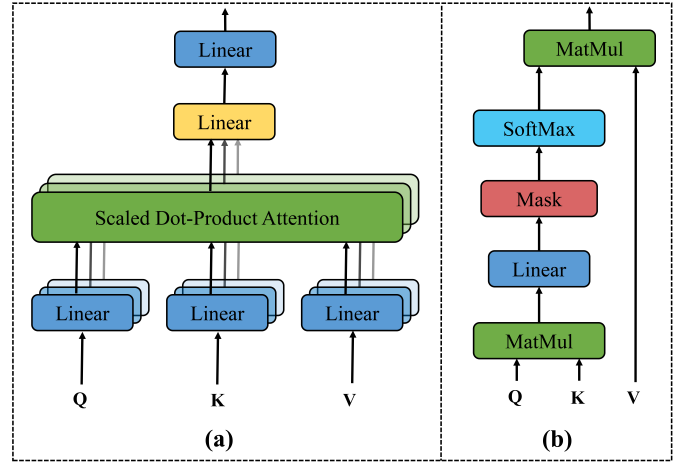


Fig. 3. Attention mechanism of the transformer. (a) Multi-head attention mechanism. (b) Self-attention mechanism.

this, a multi-output constraint module is proposed. This module sends the Transformer encoder and CNN branches, along with fused high-level semantic features, to the softmax activation function for classification. Furthermore, by utilizing the categorical cross-entropy loss function, the losses of these features are incorporated into the overall loss calculation and constrained during backpropagation (as illustrated in Fig. 4).

## IV. EXPERIMENT AND ANALYSIS

To validate the proposed CTDBNet method's superiority, it is compared with multiple state-of-the-art RF [60], SVM [61], 2D-CNN [18], 3D-CNN [18], Resnet [49], ViT [26], SS-FTT [62] and CTMixer [56] approaches on three large-scale datasets, namely, WHU-Hi-LongKou, WHU-Hi-HanChuan and WHU-Hi-HongHu.

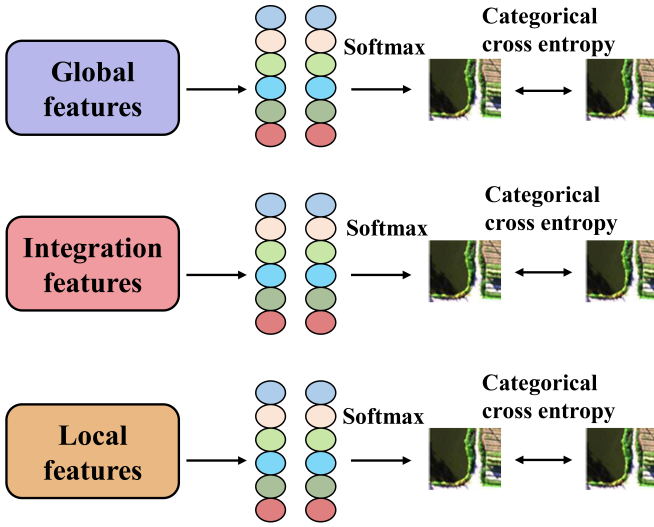


Fig. 4. Multi-Output Constraint Module.

### A. Datasets

This study used the publicly available HSI datasets. The WHU-Hi dataset [63, 64] produced by Wuhan University from a research study located on the Jiangnan plain of Hubei Province, China, with flat topography and abundant crop species (Fig. 5).

The WHU-Hi LongKou dataset was acquired using the Headwall Nano-Hyperspec unmanned aerial UAV in LongKou town, Hubei Province, China, on July 17, 2018. The image size is 550×400 pixels, with 270 bands between 400 nm and 1000 nm, and a spatial resolution of approximately 0.463 m. The study area includes 9 land cover types. The image cube and ground-truth image are shown in Fig. 5a.

The WHU-Hi HanChuan dataset was acquired using the Headwall Nano-Hyperspec unmanned aerial vehicle hyperspectral imager in Hanchuan City, Hubei Province, China, on June 17, 2016. The image size is 1217×303 pixels, with 274 bands between 400 and 1000 nm and a spatial resolution of approximately 0.109 m. The study area includes 16 land cover types. The image cube and ground-truth image are shown in Fig. 5b.

The WHU-Hi HongHu dataset was acquired using the Headwall Nano-Hyperspec unmanned aerial vehicle hyperspectral imager in Honghu City, Hubei Province, China, on November 20, 2017. The image size is 940×475 pixels, with 270 bands between 400 and 1000 nm and a spatial resolution of approximately 0.043 m. The study area includes 22 land cover types. The image cube and ground-truth image are shown in Fig. 5c.

Table I lists the overall crop category names, number of training samples, and number of test samples for these three datasets. Each dataset is divided into training and sample sets, with 0.5 % randomly selected from the total samples as the training set.

### B. Evaluation Metrics

This study uses overall classification accuracy (OA), average classification accuracy (AA), kappa coefficient, and accuracy under individual categories as evaluation metrics. It also visually presents classification diagrams as a visualization of the results.

### C. Experimental Setup

The experiment utilized the SITHOLY IW4202 rack server, equipped with an Intel® Xeon® CPU E5-2620 v4 @ 2.10GHz and four NVIDIA TITAN Xp GPUs, each with 12 GB of memory and a total of 128 GB running memory. The software platform included Ubuntu 16.04.6 LTS 64-bit OS, CUDA Toolkit 10.1, CUDNN v7.6.5, Python 3.8, and Pytorch 1.7.0. Each experiment was repeated ten times independently, with the average value taken as the final result to mitigate the impact of random factors. The number of iterations was set to 100, using cross-entropy loss as the loss function and the Adam optimizer for model optimization.

The network, which combines CNN and Transformer, emphasizes global spatial information. To investigate the impact of various input image patch sizes ( $s$ ) on classification performance, experiments were conducted using image patch sizes ranging from 5 to 15 on three datasets, with adjacent spatial sizes differing by 2. The experimental results are illustrated in Fig. 6. The figure demonstrates that the classification accuracy of the WHU-Hi LongKou dataset increases as the input image  $s$  increases. OA initially increases and then stabilizes. The WHU-Hi HanChuan and WHU-Hi HongHu datasets exhibit greater sensitivity to different input image patch sizes, with OA initially increasing and then decreasing with  $s$ . When  $s = 13$ , the OA of all three datasets approaches the maximum value. Consequently,  $s = 13$  is chosen as the input image block size for the network proposed in this study.

In order to determine the optimal configuration of the proposed network architecture in terms of learning rate and batch size, a series of targeted experiments were conducted. The experimental results are illustrated in Fig. 7, with 7(a)-(c) representing the WHU-Hi LongKou, WHU-Hi HanChuan, and WHU-Hi HongHu datasets. Different colors in the figures indicate various ranges of OA. It is evident that different learning rates and batch sizes result in different OA values for the same dataset. For the WHU-Hi LongKou dataset (7a), the impact of learning rate and batch size on OA is minimal, but there is some interaction between the two. The optimal learning rate and batch size were found to be  $1e-3$  and 100, respectively. On the other hand, the WHU-Hi HanChuan and WHU-Hi HongHu datasets show significant sensitivity to learning rate due to variations in crop types used for training. Increasing the learning rate initially boosts OA and then decreases, while increasing the batch size also shows a similar trend. For the WHU-Hi HanChuan dataset (7b), a batch size of 100 resulted in improved classification performance with the selected learning rate. Similarly, for the WHU-Hi HongHu dataset (7c), the best classification performance was achieved with a learning rate of  $1e-3$  and a batch size of 100.

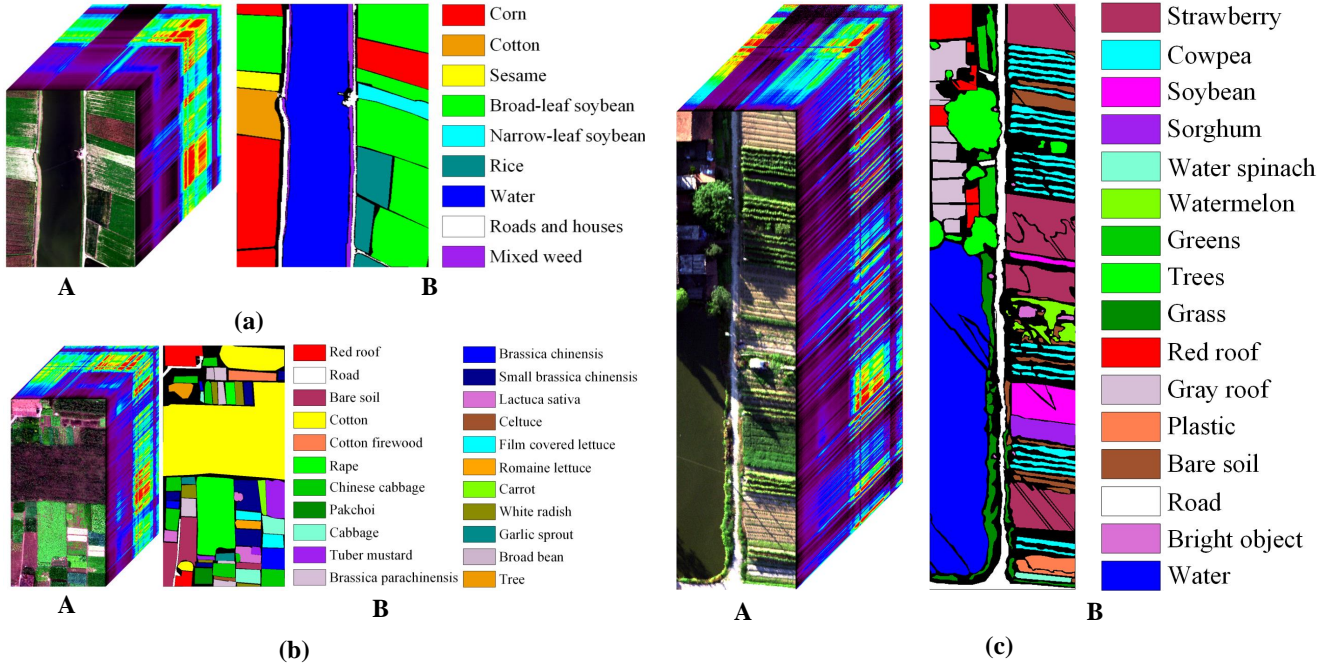


Fig. 5. Wuhan UAV-borne hyperspectral image. A and B denote Image cube and Ground-truth image respectively. (a) WHU-Hi-LongKou dataset. (b) WHU-Hi-HanChuan dataset. (c) WHU-Hi-HongHu dataset.

TABLE I  
TRAINING AND TEST SAMPLE NUMBERS IN THE WHU-HI LONGKOU DATASET, THE WHU-HI HANCHUAN DATASET, AND THE WHU-HI HONGHU DATASET

NO.	WHU-Hi LongKou			WHU-Hi HanChuan			WHU-Hi HongHu		
	Class	Training	Test	Class	Training	Test	Class	Training	Test
1	Corn	172	34339	Strawberry	223	44521	Red roof	70	13971
2	Cotton	41	8333	Cowpea	113	22640	Road	17	3495
3	Sesame	15	3016	Soybean	51	10236	Bare soil	109	21712
4	Broad-leaf soybean	316	62896	Sorghum	26	5327	Cotton	816	162469
5	Narrow-leaf soybean	20	4131	Water spinach	6	1194	Cotton firewood	31	6187
6	Rice	59	11795	Watermelon	22	4511	Rape	222	44335
7	Water	335	66721	Greens	29	5974	Chinese cabbage	120	23983
8	Roads and houses	35	7089	Trees	89	17889	Pakchoi	20	4034
9	Mixed weed	26	5203	Grass	47	9422	Cabbage	54	10765
10				Red roof	52	10464	Tuber mustard	61	12333
11				Gray roof	84	16827	Brassica parachinensis	55	10960
12				Plastic	18	3661	Brassica chinensis	44	8910
13				Bare soil	45	9071	Small Brassica chinensis	112	22395
14				Road	92	18468	Lactuca sativa	36	7320
14				Bright object	5	1131	Celtuce	5	997
16				Water	377	75024	Film covered lettuce	36	7226
17							Romaine lettuce	15	2995
18							Carrot	16	3201
19							White radish	43	8669
20							Garlic sprout	17	3469
21							Broad bean	6	1322
22							Tree	20	4020
/	Total	1019	203523	Total	1289	256241	Total	1925	384678

Consequently, based on the parameter experiments, the optimal learning rate and batch size for the proposed classification network were determined to be  $1e-3$  and 100, respectively.

This study investigates how the number of encoder layers and attention heads can impact the model's robustness and stability. Experimental results, as shown in Fig. 8, demonstrate the effects on the WHU-Hi LongKou, WHU-Hi HanChuan,

and WHU-Hi HongHu datasets. The histograms in 8(a)-(c) reveal that the differences in OA histograms across different layers and heads are minimal, with OAs remaining stable within specific ranges: LongKou: 99.52-99.68, HanChuan: 97.42-97.59, HongHu: 98.51-98.62. To ensure uniformity in the network structure across all datasets, this study opts for the CTDBNet with one transformer layer and four attention

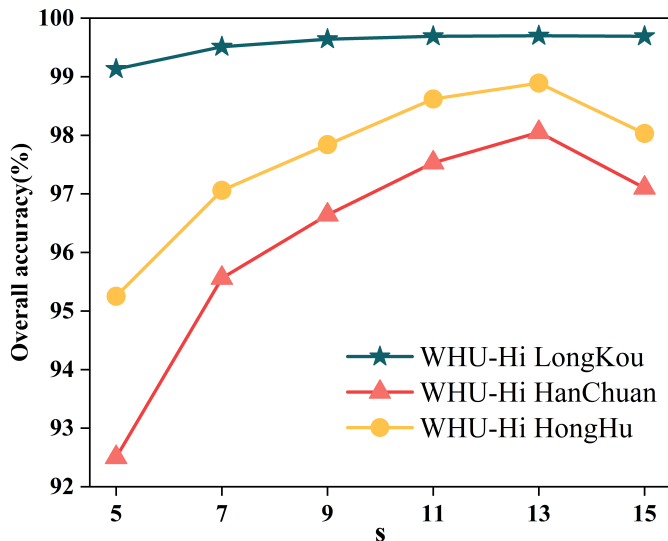


Fig. 6. Impact of different input space sizes on OA.

heads as the final network configuration.

#### D. Comparison of Experimental Results with SOTA

The OA, AA, and Kappa values of CTDBNet and other comparative methods on the WHU-Hi LongKou, WHU-Hi HanChuan, and WHU-Hi HongHu datasets are presented in Table II, III and IV, accompanied by visual representations in Fig. 9, 10 and 11. The best values are highlighted in bold in the tables, clearly indicating the superior performance of the proposed CTDBNet method. Analysis of Table II reveals that CTDBNet excels in capturing both global and local spectral features of hyperspectral imaging separately, effectively integrating high-dimensional information to achieve outstanding classification results across different land cover targets. When compared to the CNN and Transformer hybrid networks SSFTT and CTMixer, CTDBNet outperforms in final classification results, showing an increase in OA of 0.21 and 0.19, respectively. This improvement can be attributed to the multi-output constraint module of CTDBNet, which optimally reallocates feature weights. However, the performance of RF and SVM could be enhanced, particularly in the classification of cotton and soybeans with limited training samples, where individual accuracies fall below 47%. Examination of Fig. 9 demonstrates that CTDBNet significantly enhances classification performance, reducing misclassifications and ensuring complete classification edges through the fusion of local-global spectral features.

The WHU-Hi HanChuan dataset captured images in the afternoon with a lower sun angle, resulting in numerous shadow patches. The classification results for the RF and SVM methods show many misclassifications. Both 2D-CNN and 3-DCNN models display significant fragmentation, highlighting the necessity for methods to enhance model generalization. The SSFTT synthesizes the use of 3D convolutional layers

and attention mechanism modules to realize the abstraction extraction of joint spatial-spectral features, effectively mitigating classification errors caused by ‘same material different spectrum, different materials same spectrum’. However, owing to its serial extraction of spatial-spectral features without effective selection, there is still a problem of performance plummeting in the classification of small-sample targets, with the OA for categories such as Watermelon and Plastic (NO.6 and 12, respectively) being only 82.42% and 77.92%. ResNet exhibits clear misclassifications of soybeans and gray rooftops. On the other hand, ViT and CTMixer methods achieve high-precision classifications overall, but errors persist in shadow-covered areas. Despite this, CTDBNet outperforms in identifying similar spectral features through multi-feature fusion extraction, leading to reduced fragmentation compared to other methods.

In the WHU-Hi HongHu dataset, traditional classification algorithms struggle with misclassifications due to slight spectral differences among crops of the same type. Specifically, Brassica parachinensis, Brassica chinensis, and Small Brassica chinensis exhibit low classification accuracy. Deep learning methods have notably enhanced hyperspectral classification over traditional approaches. However, 2D-CNN and 3D-CNN tend to only capture local features in hyperspectral images, resulting in fragmented classification outcomes. The ViT model, on the other hand, leverages global perceptual spectral features to mitigate this fragmentation. While models like SSFTT and CTMixer combine CNN and Transformer architectures to effectively utilize spectral-spatial information for improved classification, they still struggle with misclassifications in land cover categories with limited samples. CTDBNet demonstrates the best effectiveness in categorizing various terrestrial objects due to its capability to capture spatial and spectral characteristics separately, and efficiently filter and integrate high-dimensional information. It delivers exceptionally good results for different categories, with OA for Red roof, Cotton, Rape, Tuber mustard, and Lactuca sativa reaching 98.32%, 99.7%, 98.98%, 98.26%, and 98.08% respectively, and the overall OA and Kappa coefficient being 98.31% and 97.87%. CTMixer focuses on the effective use of global and local multi-scale features, achieving better outcomes in mixed terrestrial feature regions, yet its OA and Kappa coefficients are reduced by 2.52% and 3.19% compared to CTDBNet. Visual and quantitative analyses reveal that CTDBNet achieves the highest accuracy and excels at classifying land cover categories with limited samples. This suggests that incorporating the multi-output constraint module can enhance the model’s robustness and stability.

#### E. Ablation Experiments

To thoroughly verify the effectiveness of the proposed method, ablation experiments were conducted on three datasets using different components of the network model. The baseline network was Transformer, with modules from CTDBNet sequentially added to assess their contributions. Five combined models were analyzed, and the impact of each component



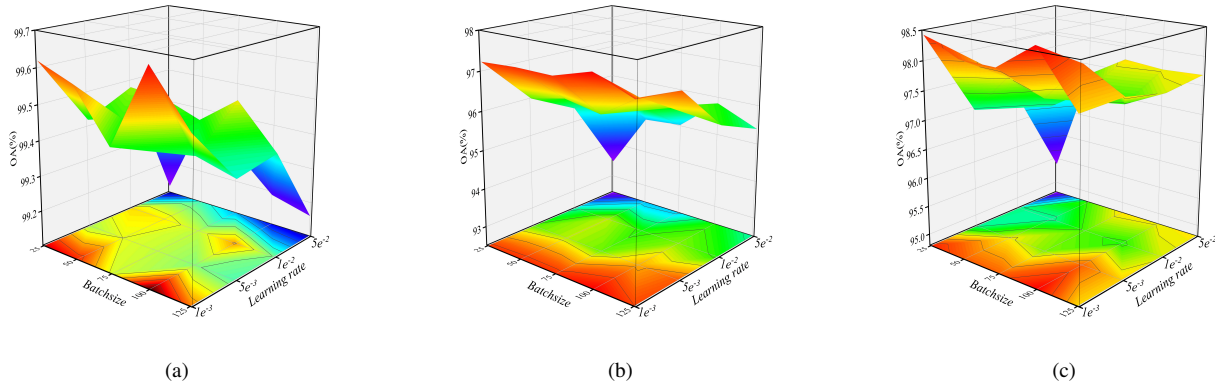


Fig. 7. Effect of different learning rates and batch sizes on performance accuracy OA. (a) Experimental results on WHU-Hi LongKou dataset. (b) Experimental results on WHU-Hi HanChuan dataset. (c) Experimental results on WHU-Hi HongHu dataset.

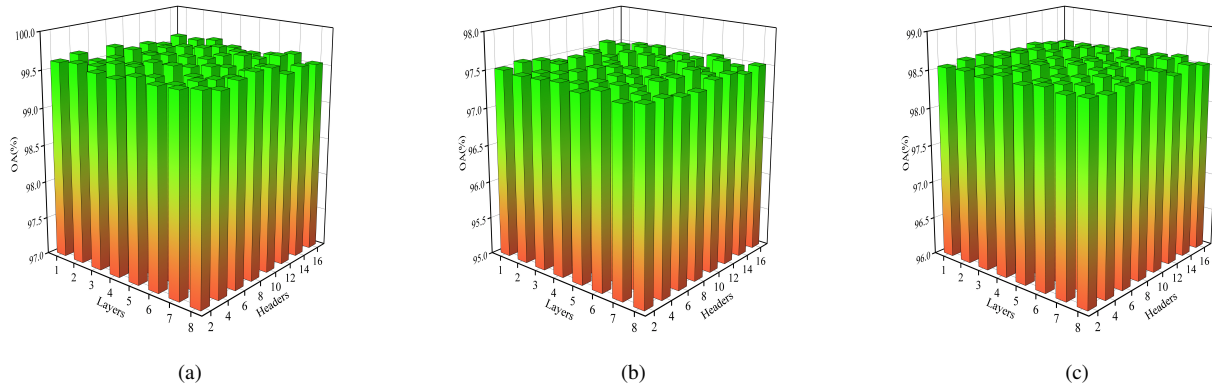


Fig. 8. OA under different numbers of transformer encoder layers and MSHA heads on (a) WHU-Hi LongKou, (b) WHU-Hi HanChuan, and (c) WHU-Hi HongHu, respectively.

TABLE II  
CLASSIFICATION PERFORMANCE OBTAINED BY DIFFERENT METHODS FOR WHU-HI LONGKOU DATASET (OPTIMAL RESULTS ARE BOLDED)

NO.	RF [60]	SVM [61]	2D-CNN [18]	3D-CNN [18]	Resnet [49]	ViT [26]	SSFTT [26]	CTMixer [56]	CTDBNet
1	89.04	90.99	94.83	98.56	88.09	92.3	99.94	99.62	<b>99.75</b>
2	45.10	46.25	58.63	65.53	89.97	72.22	98.32	<b>99.69</b>	99.53
3	90.23	89.87	95.47	97.73	88.31	97.63	99.93	<b>100.00</b>	99.83
4	87.56	87.83	84	93.91	90.07	90.15	99.36	99.31	<b>99.67</b>
5	32.59	42.57	55.11	75.11	86.88	92.35	<b>98.94</b>	98.38	98.61
6	83.85	85.18	90.79	96.62	85.26	85.53	99.89	<b>99.95</b>	99.94
7	86.86	86.83	97.66	97.61	86.83	86.65	<b>99.90</b>	99.79	99.84
8	64.61	65.55	66.35	81.44	82.83	81.71	95.6	95.51	<b>99.32</b>
9	44.06	65.87	71.83	90.21	84.56	87.58	95.1	97.83	<b>98.55</b>
OA(%)	84.65	85.21	88.75	93.93	90.43	94.05	99.37	99.39	<b>99.58</b>
AA(%)	75.33	75.26	79.41	88.53	90.68	93.84	97.66	97.60	<b>98.62</b>
k×100	86.24	87.56	85.36	92.38	88.67	94.99	99.18	99.20	<b>99.45</b>

on the OA was measured. The results of all ablation experiments are presented in Table V. The checkmark symbol “√” indicates module usage, while the cross symbol “×” indicates non-usage. Analysis revealed that using only the Transformer module resulted in relatively low OAs across the datasets, suggesting its limitations in extracting local features for hyperspectral image classification. Addition of the spectral-

spatial feature extraction module in Case 2 and Case 3 led to an increase in OA. Case 4 introduced a CNN branch in parallel with the Transformer branch to enhance local feature extraction, resulting in a significant OA improvement. Case 5 further improved the integration of features from each branch by incorporating the multi-output constraint module. Experimental findings demonstrated that Case 5 consistently

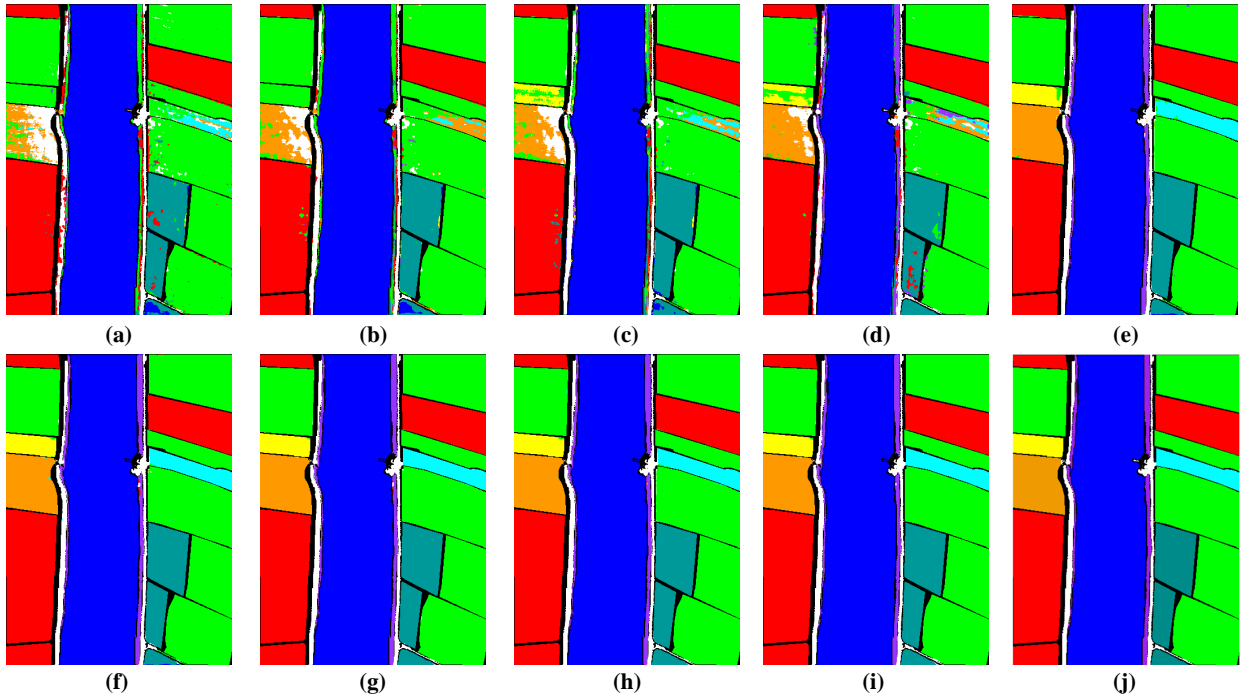


Fig. 9. Classification visualization maps of all methods on the WHU-Hi LongKou dataset. (a)–(i) Classification map of RF, SVM, 2-DCNN, 3-D CNN, Resnet, ViT, SSFTT, SSTN, CTMixer, and CTDBNet, respectively. (j) Real ground feature map.

TABLE III  
CLASSIFICATION PERFORMANCE OBTAINED BY DIFFERENT METHODS FOR WHU-HI HANCHUAN DATASET (OPTIMAL RESULTS ARE BOLDED)

NO.	RF [60]	SVM [61]	2D-CNN [18]	3D-CNN [18]	Resnet [49]	ViT [26]	SSFTT [26]	CTMixer [56]	CTDBNet
1	77.94	70.74	94.72	87.16	86.61	90.87	95.97	95.65	<b>96.09</b>
2	72.55	49.21	87.18	93.39	78.74	75.90	<b>97.90</b>	95.60	97.66
3	38.76	71.1	91.33	87.66	87.35	89.31	<b>95.54</b>	92.16	94.30
4	86.13	94.12	94.25	92.53	90.35	92.67	94.72	98.24	<b>98.28</b>
5	14.23	81.35	94.39	64.22	89.68	85.3	84.03	97.41	<b>98.35</b>
6	22.75	47.53	64.42	75.41	85.02	83.37	82.82	89.89	<b>96.11</b>
7	49.02	88.82	85.59	74.36	86.40	85.21	85.84	89.16	<b>96.29</b>
8	35.31	59.46	85.32	90.43	77.78	77.02	85.92	91.18	<b>94.63</b>
9	87.62	61.63	84.18	87.84	87.43	80.21	81.32	89.64	<b>92.70</b>
10	87.94	87.94	89.44	95.32	87.03	88.86	97.62	<b>98.39</b>	98.15
11	47.85	92.05	91.35	89.71	90.06	86.84	92.04	95.59	<b>96.86</b>
12	26.17	61.61	55.8	75.31	85.87	84.86	77.92	93.41	<b>97.30</b>
13	68.66	56.39	71.28	82.21	84.09	80.36	87.63	88.39	<b>94.25</b>
14	95.06	63.48	86.77	89.09	83.73	83.79	89.98	92.84	<b>97.96</b>
15	38.07	70.93	36.68	89.65	90.54	88.46	90.6	<b>97.10</b>	96.01
16	93.25	94	94.72	97.79	89.57	91.07	99.66	99.36	<b>99.79</b>
OA(%)	71.03	76.05	89.47	91.03	87.36	92.86	94.17	95.54	<b>97.29</b>
AA(%)	69.83	71.9	81.71	85.35	81.33	84.67	87.22	89.34	<b>94.01</b>
k $\times$ 100	70.71	72.58	88.52	89.43	85.04	91.63	93.18	94.77	<b>96.83</b>

outperformed Case 4 on all three datasets, highlighting the effectiveness of the Multi-Output Constraint Module (MOCM).

## V. CONCLUSION

In order to enhance the precision and efficiency of crop classification in areas with imbalanced samples and diverse land cover types, this study introduces a novel method called

CTDBNet. This method incorporates a dual-branch structure featuring parallel CNN and Transformer components, enabling the extraction of local-global features from hyperspectral images. A convolutional layer combination spectral-spatial feature extraction module is employed to capture low-level spectral-spatial features, while a multi-output constraint module effectively addresses information loss post multi-scale feature fusion. Experimental results demonstrate the method's

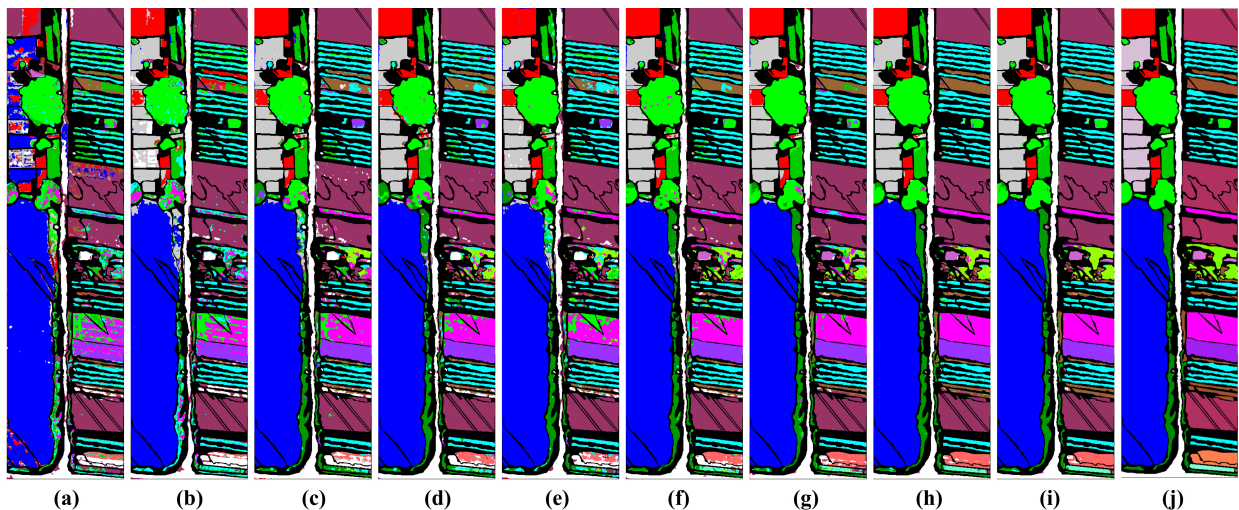


Fig. 10. Classification visualization maps of all methods on the WHU-Hi HanChuan dataset. (a)–(i) Classification map of RF, SVM, 2-DCNN, 3-D CNN, Resnet, ViT, SSFTT, SSTN, CTMixer, and CTDBNet, respectively. (j) Real ground feature map.

TABLE IV  
CLASSIFICATION PERFORMANCE OBTAINED BY DIFFERENT METHODS FOR WHU-HI HONGHU DATASET (OPTIMAL RESULTS ARE BOLDED)

NO.	RF [60]	SVM [61]	2D-CNN [18]	3D-CNN [18]	Resnet [49]	ViT [26]	SSFTT [26]	CTMixer [56]	CTDBNet
1	92.35	83.93	85.67	94.6	98.25	97.22	96.23	96.90	<b>98.32</b>
2	49.67	97.34	76.96	85.17	80.08	<b>98.62</b>	81.87	90.30	96.14
3	97.97	72.85	98.08	98.62	<b>99.96</b>	99.31	92.19	92.81	97.31
4	96.20	78.96	92.83	97.48	99.75	98.43	98.89	98.96	<b>99.79</b>
5	22.34	77.25	67.59	80.09	51.02	72.64	84.47	91.17	<b>97.60</b>
6	22.91	81.95	82.35	76.71	80.21	87.18	98.51	97.68	<b>98.98</b>
7	46.88	59.25	62.94	92.24	82.01	92.70	88.21	91.71	<b>94.41</b>
8	14.44	41.63	49.68	40.38	39.35	63.25	92.35	88.71	<b>96.23</b>
9	82.68	90.86	86.23	100	99.79	<b>100.00</b>	97.33	97.93	97.92
10	30.46	54.08	84.83	59.51	76.25	86.25	94.62	94.13	<b>98.26</b>
11	14.36	48.31	73.53	85.25	83.84	82.45	89.34	92.65	<b>96.54</b>
12	14.46	61.31	64.91	67.92	38.14	48.18	90.25	87.4	<b>98.36</b>
13	21.21	49.86	43.02	30.89	29.95	38.6	90.8	87.79	<b>96.25</b>
14	57.30	63.78	62.46	59.17	94.37	94.02	<b>98.37</b>	98.19	98.08
15	9.90	85.92	58.00	76.92	<b>100.00</b>	95.24	90.14	99.01	97.70
16	78.29	78.01	99.17	96.25	98.94	98.55	97.76	96.65	<b>99.10</b>
17	57.71	70.65	100	91.51	84.27	99.49	80.68	91.45	<b>99.73</b>
18	18.07	79.24	82.63	67.70	56.69	63.49	95.21	94.07	<b>97.29</b>
19	47.87	68.22	78.91	53.06	71.58	63.06	95.20	93.90	<b>97.99</b>
20	26.86	77.85	17.87	72.76	69.72	81.72	84.9	87.67	<b>96.31</b>
21	16.52	74.67	<b>98.78</b>	48.80	55.00	92.77	84.13	66.16	90.86
22	10.14	81.14	74.64	54.84	47.99	46.55	92.76	90.17	<b>95.91</b>
OA(%)	54.06	73.55	87.81	89.48	85.14	91.53	95.56	95.79	<b>98.31</b>
AA(%)	49.32	71.23	82.14	85.99	83.54	87.26	89.02	89.58	<b>95.26</b>
k×100	52.38	68.05	86.63	88.20	84.43	91.51	94.37	94.68	<b>97.87</b>

TABLE V  
IMPACT OF DIFFERENT MODULES ON NETWORK OA VALUE (%)

Case	CNN Branch	Conv3D	Conv2D	MOCM	LongKou	HanChuan	HongHu
1	×	×	×	×	94.97	92.86	91.53
2	✓	×	×	×	96.25	95.21	93.89
3	✓	✓	×	×	98.77	95.76	95.34
4	✓	✓	✓	✓	99.12	96.05	97.29
5	✓	✓	✓	✓	<b>99.58</b>	<b>97.29</b>	<b>98.31</b>

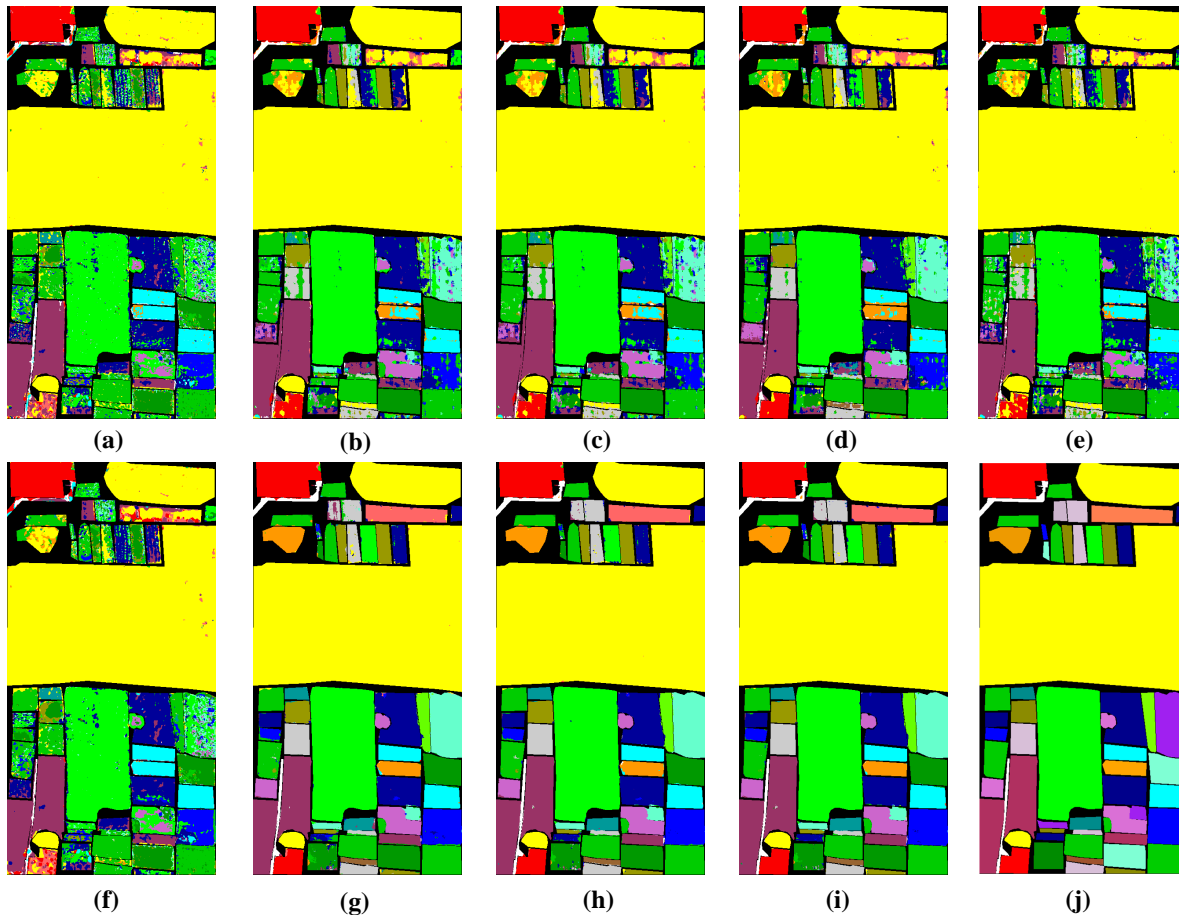


Fig. 11. Classification visualization maps of all methods on the WHU-Hi HanChuan dataset. (a)–(i) Classification map of RF, SVM, 2-DCNN, 3-D CNN, Resnet, ViT, SSFTT, SSTN, CTMixer, and CTDBNet, respectively. (j) Real ground feature map.

effectiveness in enhancing classification performance. Future research will focus on developing an HIS classification method based on Transformer to extract more representative semantic features from limited labeled samples, thereby reducing the model’s dependence on large training datasets.

#### REFERENCES

- [1] M. Weiss, F. Jacob, and G. Duveiller, “Remote sensing for agricultural applications: A meta-review,” *Remote sensing of environment*, vol. 236, p. 111402, 2020.
- [2] M. J. Khan, H. S. Khan, A. Yousaf, K. Khurshid, and A. Abbas, “Modern trends in hyperspectral image analysis: A review,” *Ieee Access*, vol. 6, pp. 14 118–14 129, 2018.
- [3] J. Hu, Z. Huang, F. Shen, D. He, and Q. Xian, “A robust method for roof extraction and height estimation,” in *IGARSS 2023-2023 IEEE International Geoscience and Remote Sensing Symposium*. IEEE, 2023.
- [4] C. Qiao, F. Shen, X. Wang, R. Wang, F. Cao, S. Zhao, and C. Li, “A novel multi-frequency coordinated module for sar ship detection,” in *2022 IEEE 34th International Conference on Tools with Artificial Intelligence (ICTAI)*. IEEE, 2022, pp. 804–811.
- [5] A. Soni, Y. Dixit, M. M. Reis, and G. Brightwell, “Hyperspectral imaging and machine learning in food microbiology: Developments and challenges in detection of bacterial, fungal, and viral contaminants,” *Comprehensive Reviews in Food Science and Food Safety*, vol. 21, no. 4, pp. 3717–3745, 2022.
- [6] F. Shen, J. Zhu, X. Zhu, J. Huang, H. Zeng, Z. Lei, and C. Cai, “An efficient multiresolution network for vehicle reidentification,” *IEEE Internet of Things Journal*, vol. 9, no. 11, pp. 9049–9059, 2021.
- [7] J. Hu, Z. Huang, F. Shen, D. He, and Q. Xian, “A bag of tricks for fine-grained roof extraction,” in *IGARSS 2023-2023 IEEE International Geoscience and Remote Sensing Symposium*. IEEE, 2023.
- [8] H. Wu, F. Shen, J. Zhu, H. Zeng, X. Zhu, and Z. Lei, “A sample-proxy dual triplet loss function for object reidentification,” *IET Image Processing*, vol. 16, no. 14, pp. 3781–3789, 2022.
- [9] R. Xu, F. Shen, H. Wu, J. Zhu, and H. Zeng, “Dual modal meta metric learning for attribute-image person re-identification,” in *2021 IEEE International Conference on Networking, Sensing and Control (ICNSC)*, vol. 1. IEEE, 2021, pp. 1–6.

- [10] M. Dalla Mura, J. A. Benediktsson, B. Waske, and L. Bruzzone, "Morphological attribute profiles for the analysis of very high resolution images," *IEEE Transactions on Geoscience and Remote Sensing*, vol. 48, no. 10, pp. 3747–3762, 2010.
- [11] P. Ghamisi, R. Souza, J. A. Benediktsson, X. X. Zhu, L. Rittner, and R. A. Lotufo, "Extinction profiles for the classification of remote sensing data," *IEEE Transactions on Geoscience and Remote Sensing*, vol. 54, no. 10, pp. 5631–5645, 2016.
- [12] A. Hennessy, K. Clarke, and M. Lewis, "Hyperspectral classification of plants: A review of waveband selection generalisability," *Remote Sensing*, vol. 12, no. 1, p. 113, 2020.
- [13] P. Ranjan and A. Girdhar, "A comprehensive systematic review of deep learning methods for hyperspectral images classification," *International Journal of Remote Sensing*, vol. 43, no. 17, pp. 6221–6306, 2022.
- [14] Y. Chen, X. Zhao, and X. Jia, "Spectral-spatial classification of hyperspectral data based on deep belief network," *IEEE journal of selected topics in applied earth observations and remote sensing*, vol. 8, no. 6, pp. 2381–2392, 2015.
- [15] H. Wu and S. Prasad, "Convolutional recurrent neural networks for hyperspectral data classification," *Remote Sensing*, vol. 9, no. 3, p. 298, 2017.
- [16] T.-H. Hsieh and J.-F. Kiang, "Comparison of cnn algorithms on hyperspectral image classification in agricultural lands," *Sensors*, vol. 20, no. 6, p. 1734, 2020.
- [17] M. Paoletti, J. Haut, J. Plaza, and A. Plaza, "Deep learning classifiers for hyperspectral imaging: A review," *ISPRS Journal of Photogrammetry and Remote Sensing*, vol. 158, pp. 279–317, 2019.
- [18] S. Bera, V. K. Shrivastava, and S. C. Satapathy, "Advances in hyperspectral image classification based on convolutional neural networks: A review." *CMES-Computer Modeling in Engineering & Sciences*, vol. 133, no. 2, 2022.
- [19] X. Xu, W. Li, Q. Ran, Q. Du, L. Gao, and B. Zhang, "Multisource remote sensing data classification based on convolutional neural network," *IEEE Transactions on Geoscience and Remote Sensing*, vol. 56, no. 2, pp. 937–949, 2017.
- [20] C. Shi, D. Liao, T. Zhang, and L. Wang, "Hyperspectral image classification based on expansion convolution network," *IEEE Transactions on Geoscience and Remote Sensing*, vol. 60, pp. 1–16, 2022.
- [21] Q. Xu, X. Yuan, C. Ouyang, and Y. Zeng, "Attention-based pyramid network for segmentation and classification of high-resolution and hyperspectral remote sensing images," *Remote Sensing*, vol. 12, no. 21, p. 3501, 2020.
- [22] M. Li, M. Wei, X. He, and F. Shen, "Enhancing part features via contrastive attention module for vehicle re-identification," in *2022 IEEE International Conference on Image Processing (ICIP)*. IEEE, 2022, pp. 1816–1820.
- [23] F. Shen, J. Zhu, X. Zhu, Y. Xie, and J. Huang, "Exploring spatial significance via hybrid pyramidal graph network for vehicle re-identification," *IEEE Transactions on Intelligent Transportation Systems*, vol. 23, no. 7, pp. 8793–8804, 2021.
- [24] J. Sun, J. Zhang, X. Gao, M. Wang, D. Ou, X. Wu, and D. Zhang, "Fusing spatial attention with spectral-channel attention mechanism for hyperspectral image classification via encoder-decoder networks," *Remote Sensing*, vol. 14, no. 9, p. 1968, 2022.
- [25] F. Shen, Y. Xie, J. Zhu, X. Zhu, and H. Zeng, "Git: Graph interactive transformer for vehicle re-identification," *IEEE Transactions on Image Processing*, 2023.
- [26] Y. Ming, N. Hu, C. Fan, F. Feng, J. Zhou, and H. Yu, "Visuals to text: A comprehensive review on automatic image captioning," *IEEE/CAA Journal of Automatica Sinica*, vol. 9, no. 8, pp. 1339–1365, 2022.
- [27] A. A. Aleissae, A. Kumar, R. M. Anwer, S. Khan, H. Cholakkal, G.-S. Xia, and F. S. Khan, "Transformers in remote sensing: A survey," *Remote Sensing*, vol. 15, no. 7, p. 1860, 2023.
- [28] J. Maurício, I. Domingues, and J. Bernardino, "Comparing vision transformers and convolutional neural networks for image classification: A literature review," *Applied Sciences*, vol. 13, no. 9, p. 5521, 2023.
- [29] W. Weng, M. Wei, J. Ren, and F. Shen, "Enhancing aerial object detection with selective frequency interaction network," *IEEE Transactions on Artificial Intelligence*, vol. 1, no. 01, pp. 1–12, 2024.
- [30] Y. Xu, H. Wei, M. Lin, Y. Deng, K. Sheng, M. Zhang, F. Tang, W. Dong, F. Huang, and C. Xu, "Transformers in computational visual media: A survey," *Computational Visual Media*, vol. 8, pp. 33–62, 2022.
- [31] W. Qi, C. Huang, Y. Wang, X. Zhang, W. Sun, and L. Zhang, "Global-local three-dimensional convolutional transformer network for hyperspectral image classification," *IEEE Transactions on Geoscience and Remote Sensing*, 2023.
- [32] F. Shen, X. Shu, X. Du, and J. Tang, "Pedestrian-specific bipartite-aware similarity learning for text-based person retrieval," in *Proceedings of the 31th ACM International Conference on Multimedia*, 2023.
- [33] H. Li, R. Zhang, Y. Pan, J. Ren, and F. Shen, "Lr-fpn: Enhancing remote sensing object detection with location refined feature pyramid network," *arXiv preprint arXiv:2404.01614*, 2024.
- [34] Y. Chen, H. Jiang, C. Li, X. Jia, and P. Ghamisi, "Deep feature extraction and classification of hyperspectral images based on convolutional neural networks," *IEEE transactions on geoscience and remote sensing*, vol. 54, no. 10, pp. 6232–6251, 2016.
- [35] J. Yue, W. Zhao, S. Mao, and H. Liu, "Spectral-spatial classification of hyperspectral images using deep convolutional neural networks," *Remote Sensing Letters*, vol. 6, no. 6, pp. 468–477, 2015.
- [36] X. Li, M. Ding, and A. Pižurica, "Deep feature fu-

- sion via two-stream convolutional neural network for hyperspectral image classification,” *IEEE Transactions on Geoscience and Remote Sensing*, vol. 58, no. 4, pp. 2615–2629, 2019.
- [37] W. Zhao and S. Du, “Learning multiscale and deep representations for classifying remotely sensed imagery,” *ISPRS Journal of Photogrammetry and Remote Sensing*, vol. 113, pp. 155–165, 2016.
- [38] J. M. Haut, M. E. Paoletti, J. Plaza, J. Li, and A. Plaza, “Active learning with convolutional neural networks for hyperspectral image classification using a new bayesian approach,” *IEEE Transactions on Geoscience and Remote Sensing*, vol. 56, no. 11, pp. 6440–6461, 2018.
- [39] Y. Li, H. Zhang, and Q. Shen, “Spectral–spatial classification of hyperspectral imagery with 3d convolutional neural network,” *Remote Sensing*, vol. 9, no. 1, p. 67, 2017.
- [40] J. Liu, K. Zhang, S. Wu, H. Shi, Y. Zhao, Y. Sun, H. Zhuang, and E. Fu, “An investigation of a multidimensional cnn combined with an attention mechanism model to resolve small-sample problems in hyperspectral image classification,” *Remote Sensing*, vol. 14, no. 3, p. 785, 2022.
- [41] J. Yang, Y.-Q. Zhao, and J. C.-W. Chan, “Learning and transferring deep joint spectral–spatial features for hyperspectral classification,” *IEEE Transactions on Geoscience and Remote Sensing*, vol. 55, no. 8, pp. 4729–4742, 2017.
- [42] S. Yu, S. Jia, and C. Xu, “Convolutional neural networks for hyperspectral image classification,” *Neurocomputing*, vol. 219, pp. 88–98, 2017.
- [43] A. Diakite, G. Jiangsheng, and F. Xiaping, “Hyperspectral image classification using 3d 2d cnn,” *Image Processing, IET*, vol. 15, no. 1, 2020.
- [44] F. Shen, M. Wei, and J. Ren, “Hsgnet: Object re-identification with hierarchical similarity graph network,” *arXiv preprint arXiv:2211.05486*, 2022.
- [45] X. Hu, X. Wang, Y. Zhong, and L. Zhang, “S3anet: Spectral-spatial-scale attention network for end-to-end precise crop classification based on uav-borne h2 imagery,” *ISPRS Journal of Photogrammetry and Remote Sensing*, vol. 183, pp. 147–163, 2022.
- [46] F. Shen, X. Du, L. Zhang, and J. Tang, “Triplet contrastive learning for unsupervised vehicle re-identification,” *arXiv preprint arXiv:2301.09498*, 2023.
- [47] J. M. Haut, M. E. Paoletti, J. Plaza, A. Plaza, and J. Li, “Visual attention-driven hyperspectral image classification,” *IEEE transactions on geoscience and remote sensing*, vol. 57, no. 10, pp. 8065–8080, 2019.
- [48] X. Tang, F. Meng, X. Zhang, Y.-M. Cheung, J. Ma, F. Liu, and L. Jiao, “Hyperspectral image classification based on 3-d octave convolution with spatial–spectral attention network,” *IEEE Transactions on Geoscience and Remote Sensing*, vol. 59, no. 3, pp. 2430–2447, 2020.
- [49] S. K. Roy, S. Manna, T. Song, and L. Bruzzone, “Attention-based adaptive spectral–spatial kernel resnet for hyperspectral image classification,” *IEEE Transactions on Geoscience and Remote Sensing*, vol. 59, no. 9, pp. 7831–7843, 2020.
- [50] D. Hong, Z. Han, J. Yao, L. Gao, B. Zhang, A. Plaza, and J. Chanussot, “Spectralformer: Rethinking hyperspectral image classification with transformers,” *IEEE Transactions on Geoscience and Remote Sensing*, vol. 60, pp. 1–15, 2021.
- [51] J. He, L. Zhao, H. Yang, M. Zhang, and W. Li, “Hsi-ibert: Hyperspectral image classification using the bidirectional encoder representation from transformers,” *IEEE Transactions on Geoscience and Remote Sensing*, vol. 58, no. 1, pp. 165–178, 2019.
- [52] Y. Qing, W. Liu, L. Feng, and W. Gao, “Improved transformer net for hyperspectral image classification,” *Remote Sensing*, vol. 13, no. 11, p. 2216, 2021.
- [53] X. Tan, K. Gao, B. Liu, Y. Fu, and L. Kang, “Deep global-local transformer network combined with extended morphological profiles for hyperspectral image classification,” *Journal of Applied Remote Sensing*, vol. 15, no. 3, pp. 038 509–038 509, 2021.
- [54] S. Mei, C. Song, M. Ma, and F. Xu, “Hyperspectral image classification using group-aware hierarchical transformer,” *IEEE Transactions on Geoscience and Remote Sensing*, vol. 60, pp. 1–14, 2022.
- [55] Z. Zhong, Y. Li, L. Ma, J. Li, and W.-S. Zheng, “Spectral–spatial transformer network for hyperspectral image classification: A factorized architecture search framework,” *IEEE Transactions on Geoscience and Remote Sensing*, vol. 60, pp. 1–15, 2021.
- [56] J. Zhang, Z. Meng, F. Zhao, H. Liu, and Z. Chang, “Convolution transformer mixer for hyperspectral image classification,” *IEEE Geoscience and Remote Sensing Letters*, vol. 19, pp. 1–5, 2022.
- [57] M. Liang, Q. He, X. Yu, H. Wang, Z. Meng, and L. Jiao, “A dual multi-head contextual attention network for hyperspectral image classification,” *Remote Sensing*, vol. 14, no. 13, p. 3091, 2022.
- [58] L. Yang, Y. Yang, J. Yang, N. Zhao, L. Wu, L. Wang, and T. Wang, “Fusionnet: a convolution–transformer fusion network for hyperspectral image classification,” *Remote Sensing*, vol. 14, no. 16, p. 4066, 2022.
- [59] X. Yang, W. Cao, Y. Lu, and Y. Zhou, “Hyperspectral image transformer classification networks,” *IEEE Transactions on Geoscience and Remote Sensing*, vol. 60, pp. 1–15, 2022.
- [60] L. Ballanti, L. Blesius, E. Hines, and B. Kruse, “Tree species classification using hyperspectral imagery: A comparison of two classifiers,” *Remote Sensing*, vol. 8, no. 6, p. 445, 2016.
- [61] Y. Chen, X. Zhao, and Z. Lin, “Optimizing subspace svm ensemble for hyperspectral imagery classification,” *IEEE Journal of Selected Topics in Applied Earth Observations and Remote Sensing*, vol. 7, no. 4, pp. 1295–1305, 2014.
- [62] L. Sun, G. Zhao, Y. Zheng, and Z. Wu, “Spectral–spatial feature tokenization transformer for hyperspectral image classification,” *IEEE Transactions on Geoscience and*

*Remote Sensing*, vol. 60, pp. 1–14, 2022.

- [63] Y. Zhong, X. Wang, Y. Xu, S. Wang, T. Jia, X. Hu, J. Zhao, L. Wei, and L. Zhang, “Mini-uav-borne hyperspectral remote sensing: From observation and processing to applications,” *IEEE Geoscience and Remote Sensing Magazine*, vol. 6, no. 4, pp. 46–62, 2018.
- [64] Y. Zhong, X. Hu, C. Luo, X. Wang, J. Zhao, and L. Zhang, “Whu-hi: Uav-borne hyperspectral with high spatial resolution (h2) benchmark datasets and classifier for precise crop identification based on deep convolutional neural network with crf,” *Remote Sensing of Environment*, vol. 250, p. 112012, 2020.